

Autonomous Scanning Probe Microscopy Investigations over WS₂ and Au{111}

John C. Thomas¹, Antonio Rossi^{1,2}, Darian Smalley³, Luca Francaviglia¹, Zhuohang Yu^{4,5}, Tianyi Zhang^{4,5}, Shalini Kumari^{4,5}, Joshua A. Robinson^{4,5}, Mauricio Terrones^{4,5,6}, Masahiro Ishigami³, Eli Rotenberg², Edward Barnard¹, Archana Raja¹, Ed Wong¹, D. Frank Ogletree¹, Marcus M. Noack⁷, and Alexander Weber-Bargioni¹

¹*Molecular Foundry, Lawrence Berkeley National Laboratory, California 94720, United States of America*

²*Advanced Light Source, Lawrence Berkeley National Laboratory, California 94720, United States of America*

³*Department of Physics, University of Central Florida, Orlando, FL 32816, United States of America*

⁴*Department of Materials Science and Engineering, The Pennsylvania State University, University Park, PA 16802 United States of America*

⁵*Center for Two-Dimensional and Layered Materials, The Pennsylvania State University, University Park, PA, 16802 United States of America*

⁶*Department of Physics and Department of Chemistry, The Pennsylvania State University, University Park, PA, 16802 United States of America*

⁷*Center for Advanced Mathematics for Energy Research Applications, Lawrence Berkeley National Laboratory, Berkeley, CA 94720, United States of America*

1 ABSTRACT

Point defect identification in two-dimensional materials enables an understanding of the local environment within a given system, where scanning probe microscopy that takes advantage of hyperspectral tunneling bias spectroscopy acquisition can both map and identify the atomic and electronic landscape. Here, dense spectroscopic volume is collected autonomously *via* Gaussian process regression, where convolutional neural networks are used in tandem for defect identification. Monolayer semiconductor is explored on sulfur vacancies within tungsten disulfide (WS₂), to provide the first two-dimensional hyperspectral insight into available sulfur-substitution sites within a transition metal dichalcogenide, which is combined with spectral confirmation on the Au{111} herringbone reconstruction for both tip state verification and local fingerprinting, where face-centered cubic and hexagonal close packed regions are detected by machine learning methods. Acquired data enable image segmentation across the above mentioned defect modes, and a workflow is provided for both machine-driven decision making during experimentation and the capability for user customization.

2 INTRODUCTION

Transition metal dichalcogenides (TMDs), such as WS₂, have gained substantial interest for point-defect control,^{1,2} serving as host substrates for quantum emitters,³ spin valley splitting properties,⁴⁻⁶ and tunable band gap engineering.⁷⁻⁹ Sulfur vacancies (V_S) can be controllably created to serve as target sites for photo- and spin- active functionalization.^{10,11} Scanning probe microscopy (SPM) can measure the electronic characteristics at the atomic level of induced defects,^{1,4,6} while also providing a path to

excite optical transitions.¹² Two-dimensional (2D) TMDs provide a wide phase space to non-destructively modify the quantum environment through strain tuning, heterostructuring, and Moiré twist angle enabling systematic studies of quantum phenomena in 2D materials that directly correlate local environment and morphology with quantum coherence and functionality.

Scanning tunneling microscopy (STM), one branch of SPM, remains fundamental for characterizing and understanding material and surface properties at distances within the atomic-to-nano range, providing information at scale into, *e.g.*, spin-orbit coupling effects within chalcogen vacancies, electrically-driven photon emission of individual defects, and substitutional fingerprinting by measuring the local density of states (LDOS).^{13–16} STM is also one of the only techniques available for purposely manipulating atoms and molecules. Since the inception of scanning tunneling spectroscopy (STS), which measures current-voltage (I/V) characteristics, the vast majority of experiments are performed using single pixel spectroscopy, where routes for data collection tend to be geometrically positioned along a line or grid during point acquisition. The first harmonic of an atomically resolved area can be measured over a defined voltage range, with lock-in techniques, that corresponds to a convolution of the tip and surface LDOS (dI/dV). Assuming the tip remains constant then the data collected is from the sample alone,¹⁷ where inelastic contributions (d^2I/dV^2) can also be inferred from the second harmonic.¹⁸ This gives insight into the electronic structure at the atomic scale with sufficient spectroscopic energy resolution to resolve quantum phase transitions, enable the exploration of next generation color centers, and capability to resolve quantum emitters at scale. Furthermore, the ability to understand the electronic structure at the atomic scale becomes increasingly important, as defects and impurities can impact the macroscopic functionality.

One technical challenge of STM/STS is the difficulty of the technique to acquire reproducible, artifact-free tunneling, especially in heterogeneous samples. Acquisition times are governed by multiple hyperparameters, such as voltage range, step size, and dwell time, where spectral collection that is both highly resolved energetically and spatially is confounded by a variety of factors, which can be very time intensive. In conventional STM/STS, point LDOS exploits the full energetic range of interest with high resolution, and a subsequent dI/dV map can then be collected at a specified energy level for high spatial resolution at the cost of greater experimental broadening. Current imaging tunneling spectroscopy (CITS) consists of scanning the tip in x - and y - directions within a predefined grid and collecting a high-resolution spectrum at each pixel.¹⁹ CITS takes advantage of both modalities to create a full spectral and spatial picture of a region of interest, but this modality is complicated by any accompanied thermal drift, piezo hysteresis, and grid optimization, which can introduce artifacts in the spectra. The need for technical approaches that make STS more accessible and user-friendly can provide essential utility into materials discovery and design.

One route to make STS more available as a tool to provide critical insight into material systems is to make use of Gaussian process (GP) regression for hyperspectral data collection,^{20–24} which is a well-known method for function approximation and uncertainty quantification. This method refers to a hash table of variables, where any finite number of which have a joint Gaussian distribution. Given some initial input, a Gaussian prior probability density function can provide a posterior mean and variance within a model, which can be used to make autonomous decisions about optimal point measurements. This has been shown to be useful for hyperspectral image reconstruction,²² autonomous synchrotron experiments,²¹ and materials discovery,²⁴ to name a few applications. The promise of autonomously driven experiments with STM come at the benefit of the human operator and can provide industrial application, where a qualified scientist or engineer can initialize an experiment and allow an artificially intelligent or machine learning (AI/ML) algorithm to complete the workflow.^{25,26} Here, we present one technical approach to address this challenge to perform STS at defect sites on two different surfaces and demonstrate a) how to perform measurements with reproducible spectra, and b) create statistically significant electronic characterization of the different intrinsic defects that can be found on samples of interest. While this does not enhance sample throughput directly, it allows for new samples to be spectroscopically and automatically interrogated in terms of defect diversity and their electronic fingerprint, such that a non-STM expert would have the ability to produce relevant spectroscopic insight

after little training. This carried is out with the combination of two machine learning techniques for autonomous experimentation, where a one-dimensional convolutional neural network (1D-CNN) is used to identify obtained spectra that is collected autonomously by a GP to obtain an accurate CITS representation at a rate that is superior to grid collection. Surface maps are obtained for chalcogen vacancies within WS₂ and between known surface reconstructions on a Au{111} surface.

3 RESULTS AND DISCUSSION

An autonomous hyperspectral STM/STS experiment can be initialized over a chalcogen vacancy (Figure 1A) within WS₂. Spatial parameters and tip offsets in both the x- and y- direction are defined by an input image that is further used in cross-correlation feature tracking (see supplemental information). At each point defined by the GP, the bias is ramped over a certain voltage range while the tip is held at constant height. Each spectra is then identified by a 1D-CNN, where class probabilities are computed and the sum of dI/dV signal intensity is input into the GP for mean and objective function calculation. As the experiment progresses, a proposed measurement is given to the instrument to collect a point at the uncertainty maximum, where the evolution of both mean and variance functions can be monitored (Fig. 1B). Sufficient chalcogen orbital information is obtained under 100 collected data points, where signal intensity over an identifiable voltage range (specific for the V_S deep in-gap state within WS₂) is monitored.⁶

The GP model can be defined for a given dataset, $D = \{\mathbf{x}_i, y_i\}$, as the probability distribution over functions $f(x)$ as

$$p(\mathbf{f}) = \frac{1}{\sqrt{(2\pi)^{dim} |\mathbf{K}|}} \exp \left[-\frac{1}{2} (\mathbf{f} - \boldsymbol{\mu})^T \mathbf{K}^{-1} (\mathbf{f} - \boldsymbol{\mu}) \right] \quad (1)$$

where, by applying the covariance kernel, \mathbf{K} is the calculated covariance matrix of D , and $\boldsymbol{\mu}$ is the prior mean vector. The likelihood over \mathbf{y} is then

$$p(\mathbf{y}) = \frac{1}{\sqrt{(2\pi)^{dim} |\mathbf{V}|}} \exp \left[-\frac{1}{2} (\mathbf{y} - \mathbf{f})^T \mathbf{V}^{-1} (\mathbf{y} - \mathbf{f}) \right] \quad (2)$$

where \mathbf{V} is the matrix of the possibly non-i.i.d. noise. From the above equations, the posterior probability distribution for a measurement outcome at \mathbf{x}_0 can be calculated. The probability distribution mean and variance functions are then defined as

$$m(\mathbf{x}_0) = \boldsymbol{\mu} + \mathbf{k}^T (\mathbf{K} + \mathbf{V})^{-1} (\mathbf{y} - \boldsymbol{\mu}) \quad (3)$$

$$\sigma^2(\mathbf{x}_0) = \mathbf{k}(\mathbf{x}_0, \mathbf{x}_0) - \mathbf{k}^T (\mathbf{K} + \mathbf{V})^{-1} \mathbf{k} \quad (4)$$

Covariances are computed by the Matérn kernel, which is commonly chosen to match physical processes.²⁷ The kernel is defined as

$$k(\mathbf{x}_i, \mathbf{x}_j) = \frac{2^{1-\nu}}{\Gamma(\nu)} \left(\frac{\sqrt{2\nu}}{l} r \right)^\nu B_\nu \left(\frac{\sqrt{2\nu}}{l} r \right) \quad (5)$$

where $r = \|\mathbf{x}_i - \mathbf{x}_j\|_{l_2}$, B_ν is the modified Bessel function, and ν is a parameter defining the differentiability. This is combined with an anisotropic kernel definition to control the level of differentiability in each direction of input space.

Bayesian optimization, where a statistical model of the system is generated based on prior data, uses an acquisition function to suggest the next point of input, which is non-trivial in its design. There are a number of acquisition functions available with different balances of exploration, with the goal to improve the statistical model, and exploitation, with the goal of utilizing the improved statistical model to find the global optimum.

Here experimental data is collected by exploration, where points are suggested to improve the Gaussian process *via* point selection at uncertainty maxima. The full energy range can be measured at each point, and indeed we can zoom into any voltage range to visualize orbital information and are able to obtain an optimized hyperspectral map with high resolution both spatially and energetically. After sufficient data points are collected, we can interpolate over 128 x 128 pixels from acquired data and compare different acquisition functions using Gaussian process upper confidence bound (GP-UCB), covariance, variance, and Shannon’s entropy (Figure S1). Here the UCB acquisition function gives the greatest correlation results on the fewest number of data points for our mean function, where greater than 95% correlation is reached after only 35 acquisition points. However, after orbital correlation reaches 95%, a covariance-driven autonomous experiment maintains the greatest correlation average with the least standard deviation (97 +/- 1.5 %) after 60 collected spectra (Figures S2-S5).

When the GP experiment is fully completed, we can successfully identify V_S compared to pristine WS_2 with a trained 1D-CNN using an 80/20 train/test split ratio on 1482 scanning tunneling spectra, consisting of 424 Au_{fcc} , 709 Au_{hcp} , 158 V_S , and 191 WS_2 spectra. Test data is further split (60/40 ratio) into a validation set used during training to give an estimate of the model’s skill and a test set used on unbiased data after training. CNN architectures have shown application towards identifying tip state on H:Si(100),²⁸ with automated hydrogen lithography,^{29,30} and in identifying adatom arrays on a $Co_3Sn_2S_2$ cleaved surface.³¹ The CNN architecture chosen uses shared weights to reduce the number of trainable parameters and extract spectral features on the pixel level, which is based on hyperspectral image classification methods used on AVIRIS sensor datasets.^{32,33}

The 1D-CNN contains two convolution layers, one dropout layer to help overcome overfitting, and one fully connected linear layer, where the softmax can then be used after training to obtain point STS class probabilities. Each convolutional layer makes use of a 1x3 kernel to compute the sliding dot product and produce spectral feature maps at each layer (stride 1, padding 1), which is followed by batch normalization, a rectified linear unit (ReLU) activation, and maxpooling layer. The pooling layer down-samples each map while retaining the most important information. ReLU is nonlinear operation that retains neuron values if it is positive or returns a zero if the input is negative, and is used on both 64 and 128 node layers. During training, the Adam algorithm³⁴ with a learning rate of 10^{-4} and computed cross-entropy loss for optimization are used to automatically identify spectral features, where the Adam optimizer minimizes loss. Input and output are shown in Figure 2, where spectroscopy over a hexagonally-closed packed region on Au{111} is input and passed through the defined network to produce class identification. Accuracy and loss are shown through 20 epochs for both training and test data, with class accuracy scores presented in Table 1 for the first six epochs. Pristine WS_2 , V_S , Au_{hcp} , Au_{fcc} training spectra are all optimized within the first 6 epochs, where the model reaches > 95% accuracy on Au_{fcc} validation data after 5 epochs and 100% accuracy on for remaining classes. Overall test performance reaches 100% accuracy after 6 epochs, which is the model chosen for classification (see supplemental information for test performance metrics). Subsequent identification over herringbone reconstruction is performed (Figure 3), where an impurity is used to track drift during a given cycle, dense hyperspectral data is classified with the 1D-CNN, and image segmentation can be performed with individually classed STS point overlays or pixel-by-pixel using an interpolated form. The peak in dI/dV at -0.48 V shows the a tendency for low energy surface-state electrons to localize in Au_{hcp} regions.¹⁶ A completed experiment over a V_S within WS_2 is also presented showing defect segmentation using the trained 1D-CNN.

Experiments are performed at liquid helium temperatures and in ultrahigh vacuum to minimize any drift during an experimental run. Furthermore, any residual drift, driven by either residual thermal fluctuations during piezo motion, sample-to-sample variability, or tool-to-tool differences, is solved by acquiring interval images at the predefined offset window and then computing feature correlation (between spectral acquisition and after $n = 10$ points) using sliding image patches (Figure S6). This block-matching approach is a common technique for image recognition and operates by taking the maximum correlation within a given pixel range.³⁵⁻³⁷ Any computed offset is registered to the tool by updating the scan window location during the autonomous hyperspectral experiment. Collected images are plane corrected with a line-by-line linear fit to adjust for tilt, since SPM tips are not always perfectly

normal to a given sample. Each high resolution spectra is swept from +1.4 V to -1.8 V on WS₂ (or +1 to -1 V on Au) and takes 2 minutes for the complete sweep. After 30 minutes, drift was measured to be on the order of $0.5 \pm 0.2 \text{ \AA}$ on WS₂ and $1.1 \pm 0.8 \text{ \AA}$ over Au{111} that is shown in Figure S7. Hyperparameters can be fine-tuned to best accommodate for any of the defined drift modes during an experiment and for subsequent reproducibility.

Where previous reports have used either spatial features, decreased pixel density in spectral space, or some combination for segmentation, we unambiguously identify defects and surface-state based on high resolution spectral features that leverage the power of Gaussian processes combined with a CNN architecture for defect prediction.

4 CONCLUSION

A method for autonomous experimentation, based on a Python-to-LabVIEW interface, is presented that makes use of both GPs and a 1D-CNN for spectral identification, which enables point defect fingerprinting across a wide variety of materials and surfaces. Image segmentation can be subsequently executed after spectral classification. As experiments can be performed without time-intensive input from the operator and at a lower spatial density, high resolution STM/STS can be performed in a high throughput fashion allowing for less redundant information over a given area of interest. Additionally, as neural network algorithms tend to require a large amount of data, the GP can be operated in exploration mode for an increased number of observations to contribute towards statistically significant measurements and ML training. We expect that the software package can find application across the scanning probe field and greatly increase experimental efficiency.

5 MATERIALS AND METHODS

5.1 Scanning probe microscopy (SPM) measurements

All measurements were performed with a Createc GmbH scanning probe microscope operating under ultrahigh vacuum (pressure $< 2 \times 10^{-10}$ mbar) at liquid helium temperatures ($T < 6 \text{ K}$). Either etched tungsten or platinum iridium tips were used during acquisition. Tip apexes were further shaped by indentations onto a gold substrate. STM images are taken in constant-current mode with a bias applied to the sample. STS measurements were recorded using a lock-in amplifier with a resonance frequency of 683 Hz and a modulation amplitude of 5 mV.

5.2 Sample Preparation

Monolayer islands of WS₂ were grown on graphene/SiC substrates with an ambient pressure CVD approach. A graphene/SiC substrate with 10 mg of WO₃ powder on top was placed at the center of a quartz tube, and 400 mg of sulfur powder was placed upstream. The furnace was heated to 900 °C and the sulfur powder was heated to 250 °C using a heating belt during synthesis. A carrier gas for process throughput was used (Ar gas at 100 sccm) and the growth time was 60 min. The CVD grown WS₂/MLG/SiC was annealed *in vacuo* at 600 °C for 30 minutes to induce sulfur vacancies.

5.3 Neural Network and Gaussian Process Implementation

The acquisition software provided leverages a Python to LabVIEW interface using the Nanonis programming interface. The GP was implemented using gpCAM (version 6.0.0), which is a library for autonomous experimentation by M. M. Noack. The CNN was constructed with Pytorch (version 1.6.0), which is a deep-learning library available in Python. The full suite of home-built software is available at <https://github.com/jthomas03/gpSTS>. An Intel Xeon E5-2623 v3 CPU with 8 cores and 64 GB of memory combined with a Tesla K80 with 4992 CUDA cores was used for training.

REFERENCES

- [1] S. Barja, S. Refaely-Abramson, B. Schuler, D. Y. Qiu, A. Pulkin, S. Wickenburg, H. Ryu, M. M. Ugeda, C. Kastl, C. Chen, C. Hwang, A. Schwartzberg, S. Aloni, S.-K. Mo, D. Frank Ogletree, M. F. Crommie, O. V. Yazyev, S. G. Louie, J. B. Neaton, and A. Weber-Bargioni, “Identifying substitutional oxygen as a prolific point defect in monolayer transition metal dichalcogenides,” *Nat. Commun.*, vol. 10, p. 3382, July 2019.
- [2] S. Wang, A. Robertson, and J. H. Warner, “Atomic structure of defects and dopants in 2D layered transition metal dichalcogenides,” *Chem. Soc. Rev.*, vol. 47, pp. 6764–6794, Aug. 2018.
- [3] A. Srivastava, M. Sidler, A. V. Allain, D. S. Lembke, A. Kis, and A. Imamoğlu, “Optically active quantum dots in monolayer WSe₂,” *Nat. Nanotechnol.*, vol. 10, pp. 491–496, June 2015.
- [4] B. Schuler, J.-H. Lee, C. Kastl, K. A. Cochrane, C. T. Chen, S. Refaely-Abramson, S. Yuan, E. van Veen, R. Roldán, N. J. Borys, R. J. Koch, S. Aloni, A. M. Schwartzberg, D. F. Ogletree, J. B. Neaton, and A. Weber-Bargioni, “How substitutional point defects in Two-Dimensional WS₂ induce charge localization, Spin-Orbit splitting, and strain,” *ACS Nano*, vol. 13, pp. 10520–10534, Sept. 2019.
- [5] J. R. Schaibley, H. Yu, G. Clark, P. Rivera, J. S. Ross, K. L. Seyler, W. Yao, and X. Xu, “Valleytronics in 2D materials,” *Nature Reviews Materials*, vol. 1, pp. 1–15, Aug. 2016.
- [6] B. Schuler, D. Y. Qiu, S. Refaely-Abramson, C. Kastl, C. T. Chen, S. Barja, R. J. Koch, D. F. Ogletree, S. Aloni, A. M. Schwartzberg, J. B. Neaton, S. G. Louie, and A. Weber-Bargioni, “Large Spin-Orbit splitting of deep In-Gap defect states of engineered sulfur vacancies in monolayer WS₂,” *Phys. Rev. Lett.*, vol. 123, p. 076801, Aug. 2019.
- [7] S. Manzeli, D. Ovchinnikov, D. Pasquier, O. V. Yazyev, and A. Kis, “2D transition metal dichalcogenides,” *Nature Reviews Materials*, vol. 2, pp. 1–15, June 2017.
- [8] K. Liu, L. Zhang, T. Cao, C. Jin, D. Qiu, Q. Zhou, A. Zettl, P. Yang, S. G. Louie, and F. Wang, “Evolution of interlayer coupling in twisted molybdenum disulfide bilayers,” *Nat. Commun.*, vol. 5, p. 4966, Sept. 2014.
- [9] C. Li, Q. Cao, F. Wang, Y. Xiao, Y. Li, J.-J. Delaunay, and H. Zhu, “Engineering graphene and TMDs based van der waals heterostructures for photovoltaic and photoelectrochemical solar energy conversion,” *Chem. Soc. Rev.*, vol. 47, pp. 4981–5037, July 2018.
- [10] E. Mitterreiter, B. Schuler, K. A. Cochrane, U. Wurstbauer, A. Weber-Bargioni, C. Kastl, and A. W. Holleitner, “Atomistic positioning of defects in helium ion treated Single-Layer MoS₂,” *Nano Lett.*, vol. 20, pp. 4437–4444, June 2020.
- [11] E. Mitterreiter, B. Schuler, A. Micevic, D. Hernangómez-Pérez, K. Barthelmi, K. A. Cochrane, J. Kiemle, F. Sigger, J. Klein, E. Wong, E. S. Barnard, K. Watanabe, T. Taniguchi, M. Lorke, F. Jahnke, J. J. Finley, A. M. Schwartzberg, D. Y. Qiu, S. Refaely-Abramson, A. W. Holleitner, A. Weber-Bargioni, and C. Kastl, “The role of chalcogen vacancies for atomic defect emission in MoS₂,” *Nat. Commun.*, vol. 12, p. 3822, June 2021.
- [12] B. Schuler, K. A. Cochrane, C. Kastl, E. S. Barnard, E. Wong, N. J. Borys, A. M. Schwartzberg, D. F. Ogletree, F. J. G. de Abajo, and A. Weber-Bargioni, “Electrically driven photon emission from individual atomic defects in monolayer WS₂,” *Sci Adv*, vol. 6, Sept. 2020.
- [13] H. J. W. Zandvliet and A. van Houselt, “Scanning tunneling spectroscopy,” *Annu. Rev. Anal. Chem.*, vol. 2, pp. 37–55, 2009.
- [14] R. J. Hamers, “Atomic-Resolution surface spectroscopy with the scanning tunneling microscope,” *Annu. Rev. Phys. Chem.*, vol. 40, pp. 531–559, Oct. 1989.

- [15] W. Peng, H. Wang, H. Lu, L. Yin, Y. Wang, B. Grandidier, D. Yang, and X. Pi, “Recent progress on the scanning tunneling microscopy and spectroscopy study of semiconductor heterojunctions,” *Small*, p. e2100655, Aug. 2021.
- [16] W. Chen, V. Madhavan, T. Jamneala, and M. F. Crommie, “Scanning tunneling microscopy observation of an electronic superlattice at the surface of clean gold,” *Phys. Rev. Lett.*, vol. 80, pp. 1469–1472, Feb. 1998.
- [17] Z. Novotny, Z. Zhang, and Z. Dohnálek, “Imaging chemical reactions one molecule at a time,” in *Encyclopedia of Interfacial Chemistry*, pp. 220–240, Elsevier, 2018.
- [18] B. C. Stipe, M. A. Rezaei, and W. Ho, “Single-molecule vibrational spectroscopy and microscopy,” *Science*, vol. 280, pp. 1732–1735, June 1998.
- [19] A. Asenjo, J. M. Gómez-Rodríguez, and A. M. Baró, “Current imaging tunneling spectroscopy of metallic deposits on silicon,” *Ultramicroscopy*, vol. 42-44, pp. 933–939, July 1992.
- [20] M. M. Noack, P. H. Zwart, D. M. Ushizima, M. Fukuto, K. G. Yager, K. C. Elbert, C. B. Murray, A. Stein, G. S. Doerk, E. H. R. Tsai, R. Li, G. Freychet, M. Zhernenkov, H.-Y. N. Holman, S. Lee, L. Chen, E. Rotenberg, T. Weber, Y. L. Goc, M. Boehm, P. Steffens, P. Mutti, and J. A. Sethian, “Gaussian processes for autonomous data acquisition at large-scale synchrotron and neutron facilities,” *Nature Reviews Physics*, pp. 1–13, July 2021.
- [21] C. N. Melton, M. M. Noack, T. Ohta, T. E. Beechem, J. Robinson, X. Zhang, A. Bostwick, C. Jozwiak, R. J. Koch, P. H. Zwart, A. Hexemer, and E. Rotenberg, “K-means-driven gaussian process data collection for angle-resolved photoemission spectroscopy,” *Mach. Learn.: Sci. Technol.*, vol. 1, p. 045015, Oct. 2020.
- [22] M. Ziatdinov, D. Kim, S. Neumayer, R. K. Vasudevan, L. Collins, S. Jesse, M. Ahmadi, and S. V. Kalinin, “Imaging mechanism for hyperspectral scanning probe microscopy via gaussian process modelling,” *npj Computational Materials*, vol. 6, pp. 1–7, Mar. 2020.
- [23] C. Williams, “Gaussian processes for machine learning.” <http://newton.cam.ac.uk/files/seminar/20070809140015001-150844.pdf>. Accessed: 2021-8-27.
- [24] M. M. Noack, G. S. Doerk, R. Li, J. K. Streit, R. A. Vaia, K. G. Yager, and M. Fukuto, “Autonomous materials discovery driven by gaussian process regression with inhomogeneous measurement noise and anisotropic kernels,” *Sci. Rep.*, vol. 10, p. 17663, Oct. 2020.
- [25] K. A. Brown, S. Brittman, N. Maccaferri, D. Jariwala, and U. Celano, “Machine learning in nanoscience: Big data at small scales,” *Nano Lett.*, vol. 20, pp. 2–10, Jan. 2020.
- [26] S. V. Kalinin, M. A. Ziatdinov, J. Hinkle, S. Jesse, A. Ghosh, K. P. Kelley, A. R. Lupini, B. G. Sumpter, and R. K. Vasudevan, “Automated and autonomous experiment in electron and scanning probe microscopy,” Mar. 2021.
- [27] C. E. Rasmussen and C. K. I. Williams, “Gaussian processes for machine learning,” 2005.
- [28] M. Rashidi and R. A. Wolkow, “Autonomous scanning probe microscopy in situ tip conditioning through machine learning,” *ACS Nano*, vol. 12, pp. 5185–5189, June 2018.
- [29] M. Rashidi, J. Croshaw, K. Mastel, M. Tamura, H. Hosseinzadeh, and R. A. Wolkow, “Deep learning-guided surface characterization for autonomous hydrogen lithography,” *Mach. Learn.: Sci. Technol.*, vol. 1, p. 025001, Mar. 2020.
- [30] A. Krull, P. Hirsch, C. Rother, A. Schiffrin, and C. Krull, “Artificial-intelligence-driven scanning probe microscopy,” *Communications Physics*, vol. 3, pp. 1–8, Mar. 2020.

- [31] K. M. Roccapiore, Q. Zou, L. Zhang, R. Xue, J. Yan, M. Ziatdinov, M. Fu, D. G. Mandrus, M. Yoon, B. G. Sumpter, Z. Gai, and S. V. Kalinin, “Revealing the chemical bonding in adatom arrays via machine learning of hyperspectral scanning tunneling spectroscopy data,” *ACS Nano*, June 2021.
- [32] A. V. Miclea, R. Terebes, and S. Meza, “One dimensional convolutional neural networks and local binary patterns for hyperspectral image classification,” in *2020 IEEE International Conference on Automation, Quality and Testing, Robotics (AQTR)*, pp. 1–6, May 2020.
- [33] G. Ortac and G. Ozcan, “Comparative study of hyperspectral image classification by multidimensional convolutional neural network approaches to improve accuracy,” *Expert Syst. Appl.*, vol. 182, p. 115280, Nov. 2021.
- [34] D. P. Kingma and J. Ba, “Adam: A method for stochastic optimization,” Dec. 2014.
- [35] J. C. Thomas, J. J. Schwartz, J. N. Hohman, S. A. Claridge, H. S. Auluck, A. C. Serino, A. M. Spokoyny, G. Tran, K. F. Kelly, C. A. Mirkin, J. Gilles, S. J. Osher, and P. S. Weiss, “Defect-Tolerant aligned dipoles within Two-Dimensional plastic lattices,” *ACS Nano*, vol. 9, pp. 4734–4742, May 2015.
- [36] J. Jain and A. Jain, “Displacement measurement and its application in interframe image coding,” *IEEE Trans. Commun.*, vol. 29, pp. 1799–1808, Dec. 1981.
- [37] N. Love and C. Kamath, “An empirical study of block matching techniques for the detection of moving objects,” 2006.

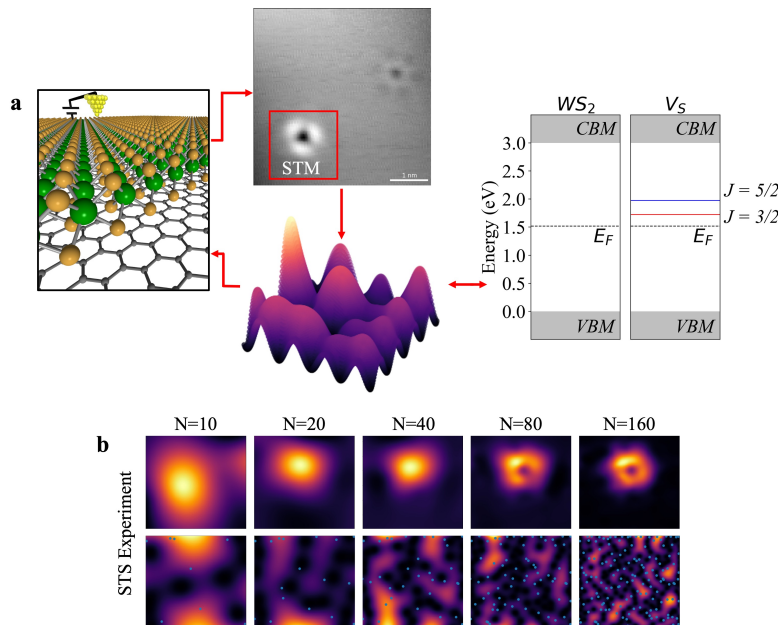


Figure 1: a) Autonomous scanning tunneling spectroscopy workflow diagram, where an input image, showing a sulfur vacancy within tungsten disulfide, is used for feature tracking and input into a Gaussian process to determine a corresponding objective and error function. The next point of measurement is taken at the uncertainty region maximum. Point defect identification is accomplished at each point and the signal summation ($0.0 \text{ V} < V_{\text{sample}} < 0.7 \text{ V}$) is used for input. B) A full autonomous experiment showing mean and covariance functions at a given interval is depicted, where orbital reconstruction is sufficiently reached with only $\sim 1\%$ of points required compared a 128×128 pixel grid experiment.

Training			
Au_{fcc}	Au_{hcp}	V_S	WS_2
63.2	49.5	43.6	64.5
98.1	98.8	93.3	97.6
98.8	99.6	99.4	100.0
95.9	98.5	97.8	98.2
100.0	99.8	100.0	99.5
100.0	100.0	100.0	100.0
Validation			
Au_{fcc}	Au_{hcp}	V_S	WS_2
100.0	24.1	0.0	100.0
95.6	98.6	95.7	100.0
100.0	96.6	100.0	100.0
88.9	100.0	100.0	100.0
95.6	100.0	100.0	100.0
95.6	100.0	100.0	100.0

Table 1: Accuracy scores of the first 6 epochs during training.

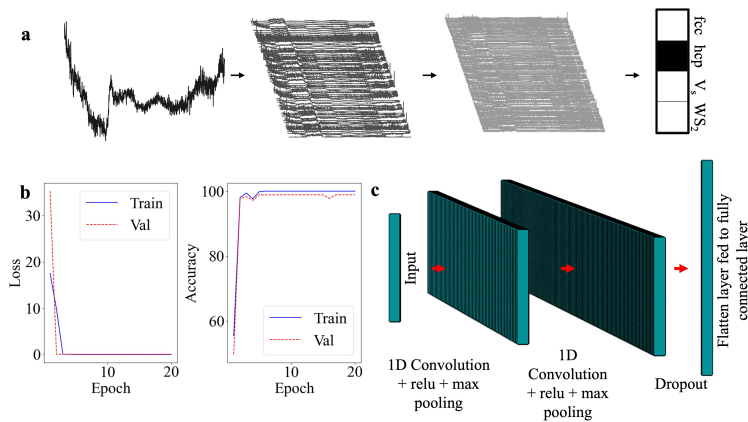


Figure 2: a) Input and output from a 1D spectra that after the first convolutional layer has a shape of 1199×64 and 1198×128 after the second layer, which is then passed through a dropout layer, flattened, and fed into a fully connected layer. Output can be subsequently fed into a soft-max layer to yield class probability, where the example spectra shown has a 100% probability to belong to the Au_{hcp} class and near zero probability for the remaining 3 classes (depicted in a gray scale) with the trained model after 6 epochs. b) Accuracy and loss after 20 training epochs is shown for completeness on both training and validation datasets. c) Schematic depicting the 1D-CNN model where each layer makes use of a rectified linear unit activation function and max pooling, which is followed by a dropout layer and fully connected layer.

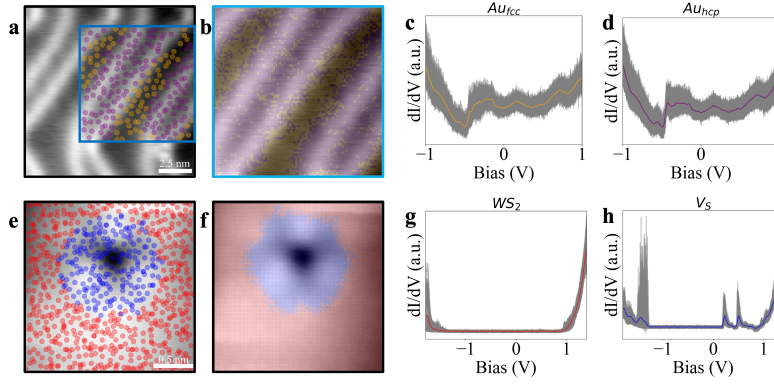


Figure 3: a) Au{111} herringbone reconstruction that is identifiable *via* point bias spectroscopy followed by classification using a trained 1D-CNN, where image tracking can be performed on a larger surface region compared to the autonomous STS experiment region. b) Data is further interpolated over a 128×128 grid, classified, and depicted as an image overlay on acquired topography ($I_{tunnel} = 30$ pA, $V_{sample} = 1$ V). Accumulated spectra over both c) Au_{fcc} and d) Au_{hcp} are shown with the mean spectrum that is colored by classification. e) V_S located within *in-situ* annealed WS_2 , where the defect itself is used for drift tracking, with overlaid acquired STS ($I_{tunnel} = 30$ pA, $V_{sample} = 1.2$ V) and f) the corresponding linear interpolated form highlighting measured in-gap states. Spectra used for training, validation, and test are shown for both g) WS_2 and h) V_S , where a total of > 1400 spectra were acquired over multiple experimental runs for both Au and WS_2 .

Autonomous Scanning Probe Microscopy Investigations over WS₂ and Au{111}

John C. Thomas¹, Antonio Rossi^{1,2}, Darian Smalley³, Luca Francaviglia¹, Zhuohang Yu^{4,5}, Tianyi Zhang^{4,5}, Shalini Kumari^{4,5}, Joshua A. Robinson^{4,5}, Mauricio Terrones^{4,5,6}, Masahiro Ishigami³, Eli Rotenberg², Edward Barnard¹, Archana Raja¹, Ed Wong¹, D. Frank Ogletree¹, Marcus M. Noack⁷, and Alexander Weber-Bargioni¹

¹*Molecular Foundry, Lawrence Berkeley National Laboratory, California 94720, United States of America*

²*Advanced Light Source, Lawrence Berkeley National Laboratory, California 94720, United States of America*

³*Department of Physics, University of Central Florida, Orlando, FL 32816, United States of America*

⁴*Department of Materials Science and Engineering, The Pennsylvania State University, University Park, PA 16802 United States of America*

⁵*Center for Two-Dimensional and Layered Materials, The Pennsylvania State University, University Park, PA, 16802 United States of America*

⁶*Department of Physics and Department of Chemistry, The Pennsylvania State University, University Park, PA, 16802 United States of America*

⁷*Center for Advanced Mathematics for Energy Research Applications, Lawrence Berkeley National Laboratory, Berkeley, CA 94720, United States of America*

CONTENTS

1	Acquisition Functions	1
2	Drift Tracking	3
3	Convolutional Neural Network Performance	5

1 ACQUISITION FUNCTIONS

The GP model prior and posterior can be used to define the acquisition function.¹ It can take a variety of forms that include measuring the total uncertainty or favor morphological features. The implemented software can include a user-defined acquisition function that passes through optimization and gives the next point of measurement for data collection. Using the GP defined joint prior given as

$$p(\mathbf{f}, \mathbf{f}_0) = \frac{1}{\sqrt{(2\pi)^{dim} |\Sigma|}} \exp \left[-\frac{1}{2} \begin{pmatrix} \mathbf{f} - \boldsymbol{\mu} \\ \mathbf{f}_0 - \boldsymbol{\mu}_0 \end{pmatrix}^T \Sigma^{-1} \begin{pmatrix} \mathbf{f} - \boldsymbol{\mu} \\ \mathbf{f}_0 - \boldsymbol{\mu}_0 \end{pmatrix} \right] \quad (1)$$

where

$$\Sigma = \begin{pmatrix} K & \boldsymbol{\kappa} \\ \boldsymbol{\kappa}^T & \mathcal{H} \end{pmatrix} \quad (2)$$

with $\kappa_i = \kappa(\phi, x_0, x_i)$, $\mathcal{K} = \kappa(\phi, x_0, x_0)$, $K_{ij} = \kappa(\phi, x_i, x_j)$, and x_0 is the point of interest. The acquisition function can now be defined as

$$f_{acq}(x) = f_{acq}(m(x), \sigma^2(x), \mathcal{K}, \Sigma(x)) \quad (3)$$

and directly provide where the next measurement point will be taken during an autonomous experiment. The simplest example of the acquisition function is the exploration method given as

$$f_{acq}(x) = \sigma^2(x) \quad (4)$$

where the posterior variance maximum is the next point of acquisition. The general definition of the acquisition function also allows for Bayesian optimization such as using the upper confidence bound (UCB) method given as

$$f_{acq}(x) = m(x) + c\sqrt{\sigma^2(x)} \quad (5)$$

and information theory methods such as the Shannon-information gain defined by

$$f_{acq}(x) = Entropy(\mathcal{K}) - Entropy(\Sigma(x)) \quad (6)$$

This can be further fine-tuned to find regions of interest, e.g. using a reference spectrum or image feature. A cost function can also be included, which defines the cost of a given measurement itself and the cost of moving within a defined parameter space.

Here we compare results from using covariance function optimization given by the Matérn kernel, the variance, UCB, and using the Shannon-information gain.

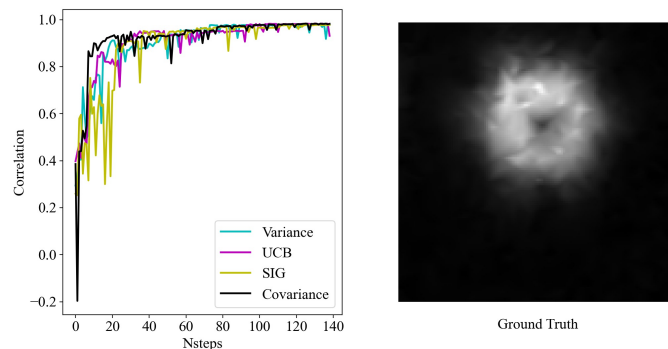


Figure S1: Correlation with ground truth data using variance, UCB, Shannon information gain (SIG), and covariance driving modes, where a linear interpolation is used to obtain a ground truth.

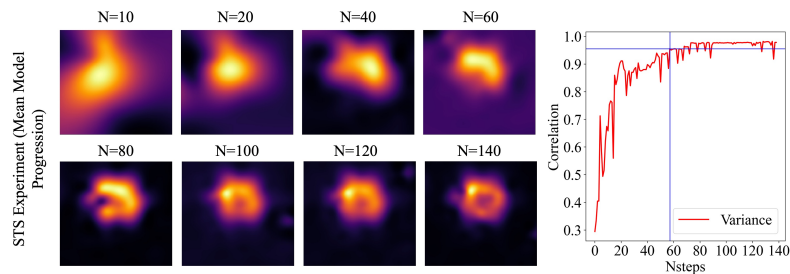


Figure S2: Variance. Correlation reaches 0.956 at 57 intervals with a mean value of 0.968 standard deviation of 0.0161.

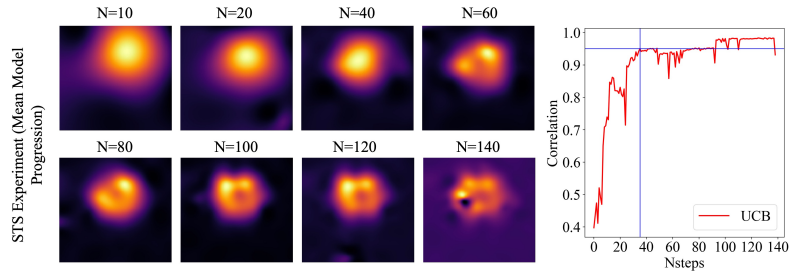


Figure S3: UCB. At 24 intervals, a sharp correlation drop is evident, where a 0.957 value with a standard deviation of 0.0236 is reached after 35 acquired points.

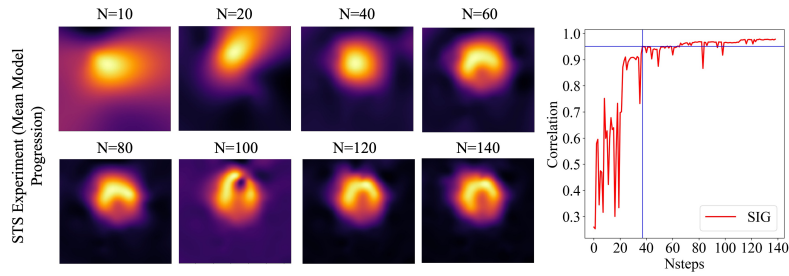


Figure S4: Shannon information gain. After 37 acquired points, a value of 0.952 is obtained with a mean value of 0.960 ± 0.0192 is maintained thereafter.

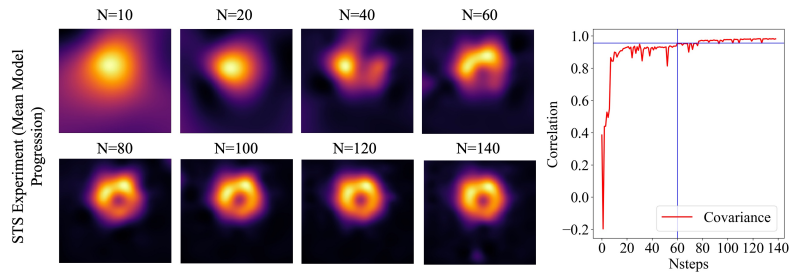


Figure S5: Covariance. A sharp upward trend in correlation is obtained after an interval value of only 7 collected points. After 60 points, a mean value of 0.969 ± 0.0152 is obtained, which arguably shows the best performance out of acquisition functions investigated.

2 DRIFT TRACKING

Drift within scanning probe microscopy techniques can be solved through a variety of methods either during the experiment or data manipulation post acquisition. Piezocreep and thermal drift are the two largest contributors to drift, where piezocreep is a nonlinear effect that can be minimized through correcting for the desired tip position to the actual tip location. However, as the piezos move or scan, some amount of thermal drift is expected. A number of image analysis methodologies that make use of features within a raster-scan image have shown efficacy in tracking drift between multiple images.² Here, we apply the same methodology towards tracking drift during point scanning tunneling spectroscopy acquisition.

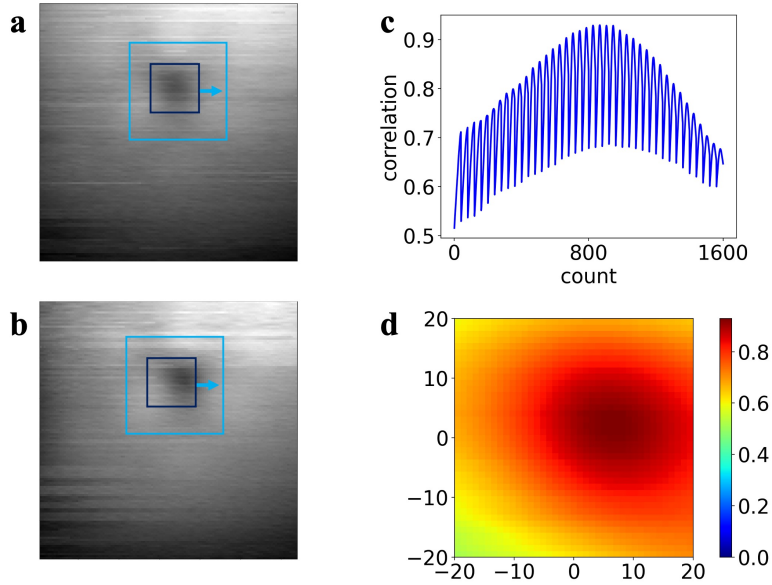


Figure S6: Cross-correlation over a sequential image taken at a) $T = 0$ and b) $T = 30$ min, where correlation is shown in both c) 1D and d) 2D, for clarity. Maximum correlation is obtained at $x_{pixel} = 5$ and $y_{pixel} = 1$, providing the offset in both the x- and y- directions between collected images.

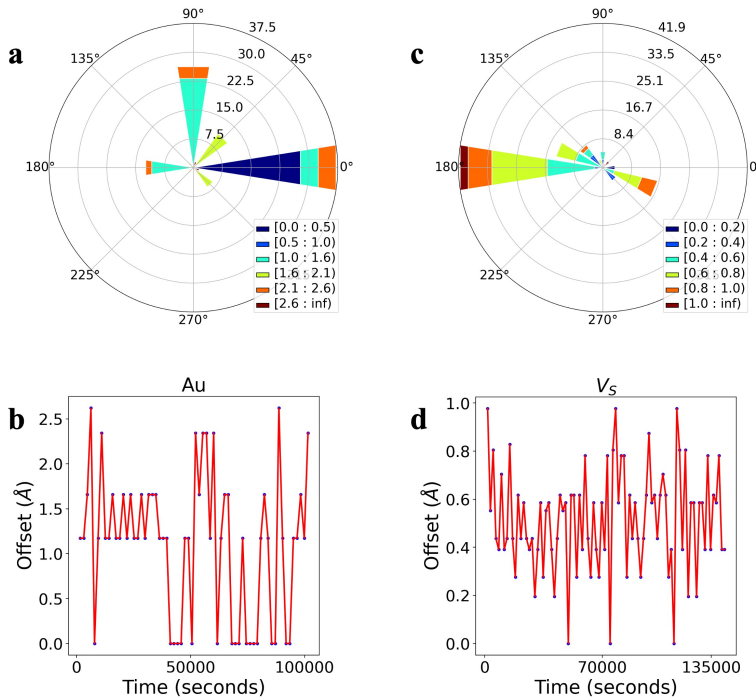


Figure S7: Computed offsets during a $\text{Au}\{111\}$ autonomous experiment is shown a) in two dimensions and b) the magnitude of the 2D vector as a function of time. Both the c) 2D and d) 1D picture are also shown for a WS_2 experiment. Drift in each example is multi-directional and highlights the need for a means to correct for any offset during measurements, however, parameters can be optimized for any possible tool-tool or run-run delta within the provided software.

3 CONVOLUTIONAL NEURAL NETWORK PERFORMANCE

Metrics from our proposed model are shown below, where we look at receiver operator characteristics to determine model performance between positive and negative classes, the confusion matrix to view sensitivity, specificity, the false negative rate, and the false positive rate, and the precision recall curve that depicts the true positive rate and the positive predictive value. In all three metrics, the model performs quite well on the data provided against four classes of spectroscopic data.

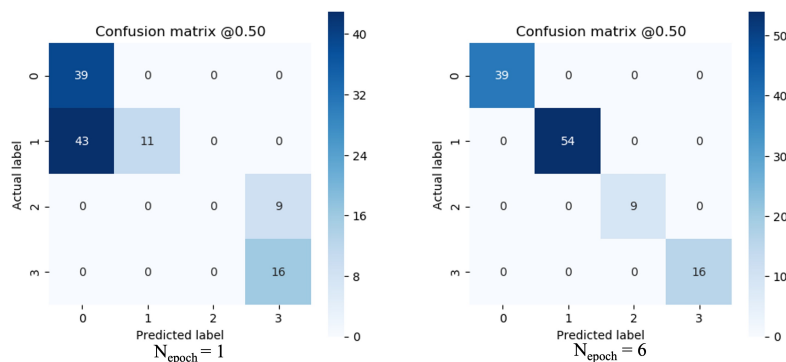


Figure S8: Confusion matrix at a threshold value of 0.5 for both the first and chosen model, where off-diagonal elements are reduced at 6 epochs.

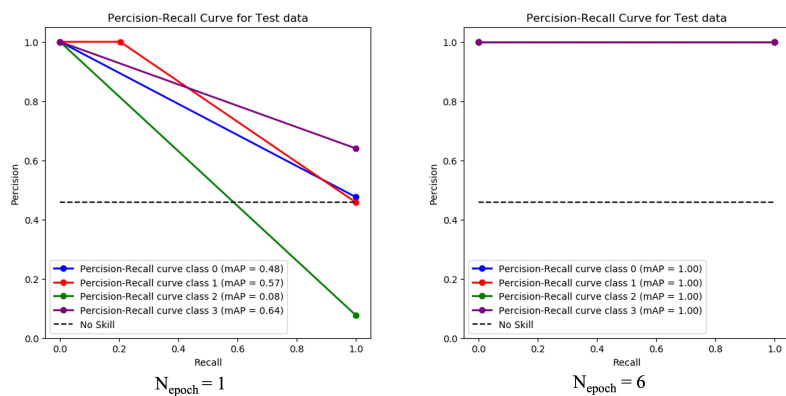


Figure S9: Precision recall curve for test data, where the mean average precision for all classes (class 0 = Au_{fcc} , class 1 = Au_{hcp} , class 3 = V_S , class 4 = WS_2) reaches 1.0 at the end of training.

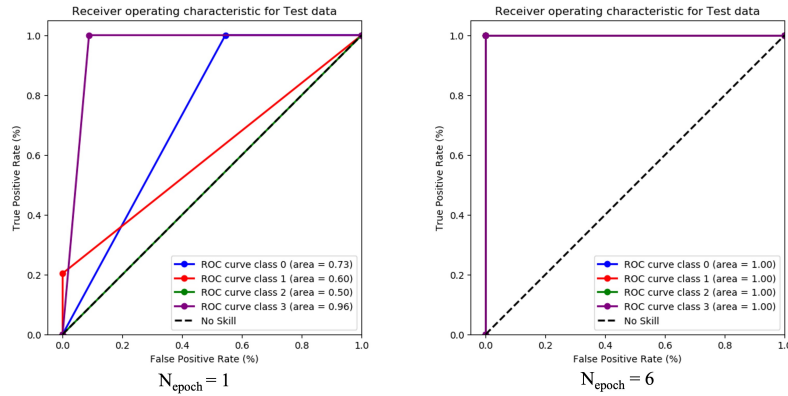


Figure S10: ROC curve for all classes, where AUC values indicate the model’s capability to distinguish between classes after the first and last epoch used in the chosen model.

REFERENCES

- [1] M. M. Noack, P. H. Zwart, D. M. Ushizima, M. Fukuto, K. G. Yager, K. C. Elbert, C. B. Murray, A. Stein, G. S. Doerk, E. H. R. Tsai, R. Li, G. Freychet, M. Zhernenkov, H.-Y. N. Holman, S. Lee, L. Chen, E. Rotenberg, T. Weber, Y. L. Goc, M. Boehm, P. Steffens, P. Mutti, and J. A. Sethian, “Gaussian processes for autonomous data acquisition at large-scale synchrotron and neutron facilities,” *Nature Reviews Physics*, pp. 1–13, July 2021.
- [2] D. A. Bonnell, D. N. Basov, M. Bode, U. Diebold, S. V. Kalinin, V. Madhavan, L. Novotny, M. Salmeron, U. D. Schwarz, and P. S. Weiss, “Imaging physical phenomena with local probes: From electrons to photons,” *Rev. Mod. Phys.*, vol. 84, pp. 1343–1381, Sep 2012.